Proximity-associated errors in contour metrology

John S. Villarrubia, Ronald G. Dixson, and András E. Vladár
National Institute of Standards and Technology, Gaithersburg, MD 20899

ABSTRACT

In contour metrology the CD-SEM (critical dimension scanning electron microscope) assigns a continuous boundary to extended features in an image. The boundary is typically assigned as a simple function of the signal intensity, for example by a brightness threshold or gradient. However, the neighborhood of different points along the feature boundary may vary considerably. Some parts of the boundary may have close neighboring features while others are relatively isolated. Neighboring features can obstruct the escape of secondary electrons. Varying proximity of neighbors therefore represents an influence on detected intensity. An intensity difference caused by a neighborhood difference can be incorrectly interpreted as a contour shift, for example when the contour passes from an isolated neighborhood to a dense one. The magnitude of this offset variation is estimated using images produced by JMONSEL, a Monte Carlo simulator of SEM secondary electron imaging, from simple model test patterns with varying neighborhoods. Similar structures were subsequently measured by both SEM and atomic force microscopy (AFM). Apparent shifts (i.e., errors) on the order of 0.5 nm to 1.0 nm for each edge were observed in both modeled and measured SEM images as compared to AFM when edge positions were assigned by using a fixed image brightness contour. Assignment of edges by brightness relative to the local background and local maximum brightness resulted in measurements that were less sensitive to neighborhood differences.

Keywords: atomic force microscopy (AFM), contour metrology, critical dimension (CD) metrology, Scanning Electron Microscopy (SEM), SEM modeling

1. INTRODUCTION

In a scanning electron microscope (SEM) image, the usual methods of assigning edge positions rely upon image processing techniques. For example, the edge might be arbitrarily assigned to the position where the intensity crosses a chosen threshold. The assigned position need not then correspond to the true edge position. The difference is an edge assignment error (Fig. 1). If the position of the edge is altered by some amount while all else remains the same, the assigned edge position will change by the same amount and the error will remain unchanged. However, the shape of the intensity profile depends upon the shape of the edge, the composition of the materials, the proximity of neighbors, and other "secondary characteristics" of the sample. If these change, the apparent position of the edge is also expected to change, even if the real position does not. Such effects, especially those corresponding to edge shape, were quantified in both simulation[1] and measurement[2,3] some time ago within the context of critical dimension measurements.

Intensity dependence upon the proximity of neighbors would be especially relevant for contour metrology. In contour metrology, the position of the edge of a feature is determined at close intervals along its perimeter. In this way, the shape of the boundary of the feature is ascertained. However, as shown in Fig. 2, the neighborhood of an edge is not constant along the perimeter of an object except in the simplest of patterns. Since the perimeter of an object in general traverses varying neighborhoods, the proximity-dependence of edge assignment errors implies that the shapes will be incorrectly determined by some amount.

The reason the intensity profile at an edge depends upon the proximity of neighbors is shown in Fig. 3. Some of the paths away from the sample, and therefore to the detector, are obstructed for electrons that emerge from an edge in close proximity to a neighboring feature. The extent of the obstruction is greater if the neighbor is larger or closer. The effects of such obstruction are easily observable in images. Figure 4, for example, compares real and simulated images of a sample

Metrology, Inspection, and Process Control for Microlithography XXIV, edited by Christopher J. Raymond,
Proc. of SPIE Vol. 7638, 76380S · © 2010 SPIE · CCC code: 0277-786X/10/$18 · doi: 10.1117/12.848406

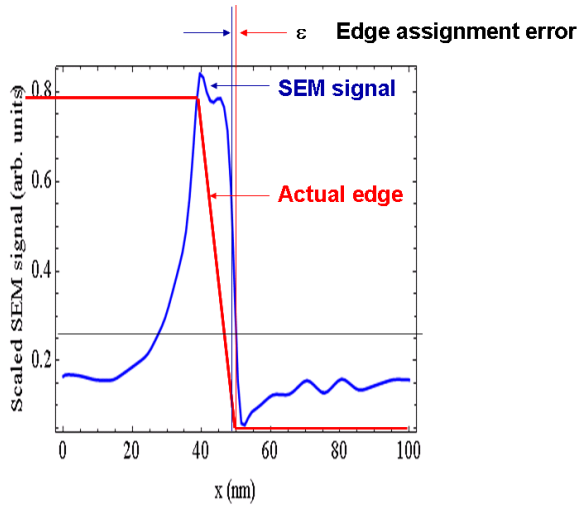

FIG. 1. Schematic showing an edge assignment error. A hypothetical trapezoidal edge and its corresponding intensity profile in the SEM are as indicated. The assigned edge differs as shown from the actual location of the edge bottom.

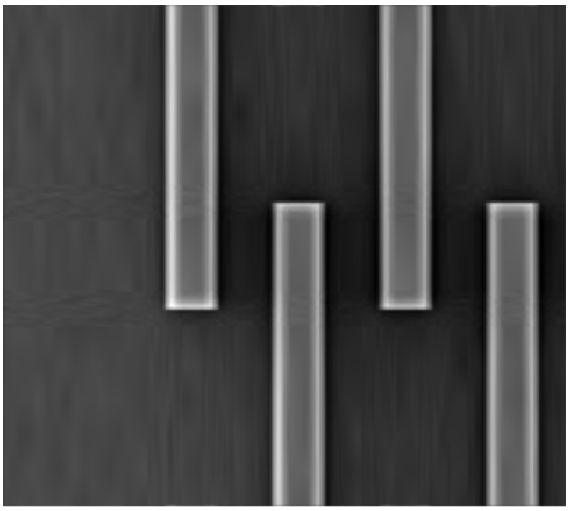

FIG. 2. Simulated SEM image of an interdigitated structure. The perimeter of any given line is sometimes nearer to, sometimes farther from, the line's neighbors.

from an intentional defect array (structures meant to qualify defect inspection tools). Confined regions like the ones labeled 3 and 3', are obviously darker than regions that are more open, like the ones labeled 1 and 1'.

The question to be answered then is not whether, but rather how much such proximity effects influence the measurement of contours. The present study was originally motivated by the observation that contours of constant intensity in Fig. 2 shifted by more than a nanometer between isolated and dense neighborhoods. The sample in Fig. 2 had been simulated for Sematech. It has features with 60 nm heights with 30 nm line- and space-widths. We set out to see whether such effects could be measured experimentally as well as in simulation and the extent to which the size of the observed metrology error was sensitive to the method of edge assignment. However, the actual sample available to us did not have 30 nm lines and spaces. It is described in the next section. Section 3 gives details of the simulation method and the results from simulation of a sample chosen to resemble our actual one. Section 4 describes our measurements, which took the form of a comparison between SEM and atomic force microscopy (AFM) measurements of our sample.

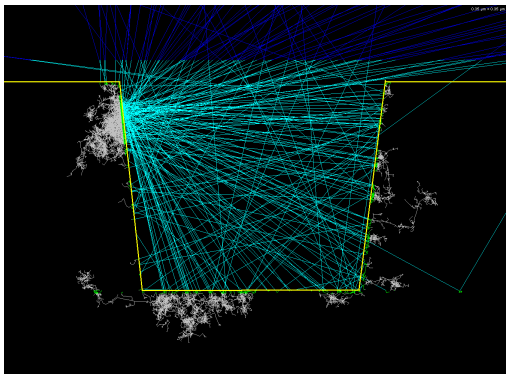

FIG. 3. Simulation of electron trajectories in a sample with an electron beam incident on the left edge of a trench. Some of the electrons that emerge from the left wall of the trench strike the neighboring wall on the right. Consequently, the number of electrons that reach the detector is reduced.

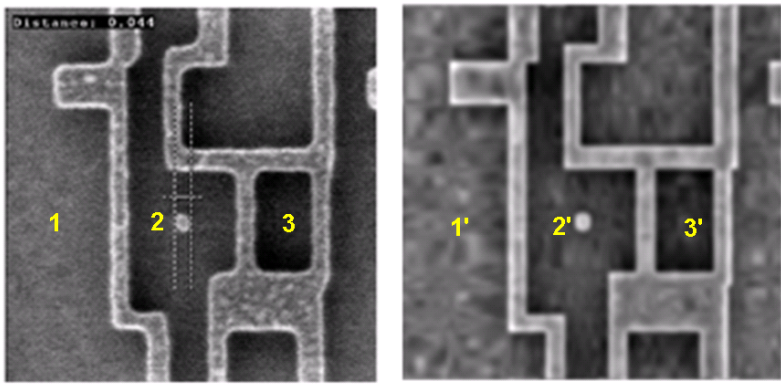

FIG. 4. Comparison of measured (left, image courtesy of ISMI) and simulated (right) images of an intentional defect array structure. Neighborhoods 1, 2, and 3 (with primes in the simulation) are progressively more confined and also progressively darker.

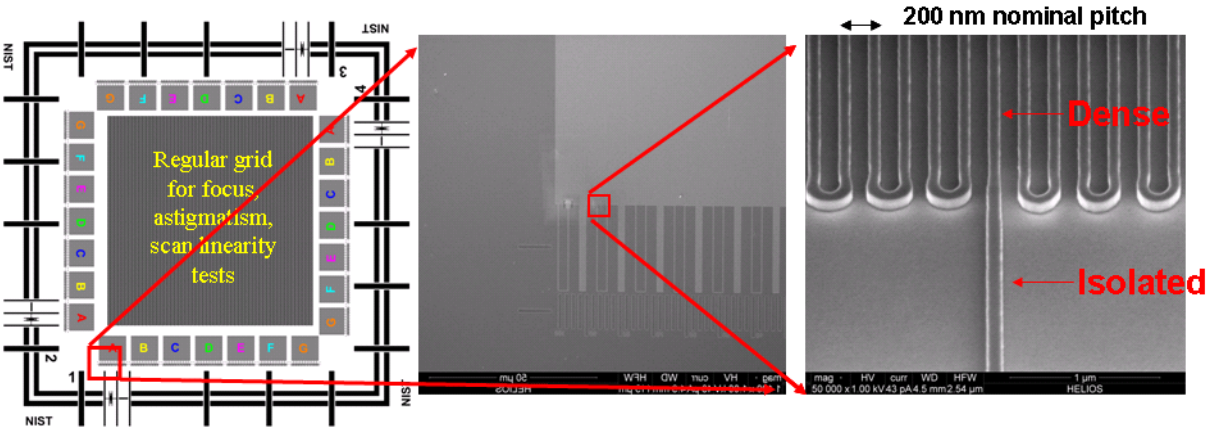

FIG. 5. Left: The NIST test pattern from the AMAG6L etched Si wafer. The target region is indicated, and an SEM micrograph of this region is shown in the middle. The pattern consists of dense lines and spaces with occasional longer lines. This particular pattern had nominally100 nm lines and spaces. The features were approximately 95 nm high. The interesting region in which the center line traverses between dense and isolated parts, is shown at the right.

2. THE SAMPLE

Measurements were performed on an etched Si sample fabricated by Sematech. The sample is designated AMAG6L. It is one of a series of samples designed by Sematech's Advanced Metrology Advisory Group (hence AMAG). The sample contains a variety of metrology test patterns, among which is one designed at NIST. This pattern is shown schematically at the left of Fig. 5. The central part of the pattern contains a regular grid that is meant for focus, astigmatism, and scan linearity tests. Next to each of the four sides of this central grid are a series of line and space gratings with varying line- and space-widths. These are labeled A through G in the schematic in the left panel of the figure. The narrowest lines and spaces are nominally 100 nm. These are in the "A" pattern, one corner of which is shown enlarged in the middle panel of the figure. (The display for this panel switches from schematic drawing to SEM image.) Some of the lines in the central periodic grating extend beyond the edge of the grating. These are more than 1 μm apart, so this part of each such line may be approximated as isolated. The final panel, on the right side of Fig. 5, shows the part of the sample where measurements were made. This is centered on the transition from isolated to dense, with field of view large enough to include both isolated and dense neighborhoods well outside of the transition region. This sample's lines were approximately 95 nm high. Thus, the ratio of line height to space width is close to 1:1, not the 2:1 ratio used in the original (Fig. 2) simulation. The actual sample therefore has a somewhat more open geometry, and we expect a correspondingly somewhat smaller iso/dense metrology difference.

3. MODELING

3.1 Physics of the model

The program organization of JMONSEL (Java Monte Carlo simulator for Secondary Electrons) was described in an earlier publication.[4] Since that publication, the physics employed in the models was changed extensively, with the introduction of a number of improved models. These models are similar in most respects to those described by Ding and Shimizu[5] and Mao et al.[6] with differences as noted by Villarrubia and Ding.[7] A summary of these models is provided here, with more attention to alterations or additions to the model since the previous publication.

The phenomena that must be modeled are elastic scattering of electrons, inelastic scattering including secondary electron generation, slowing down of the electrons through energy loss, and scattering of electrons by the potential energy change at interfaces between materials or between the sample and vacuum.

Elastic scattering refers to scattering events in which the primary electron loses negligible energy. Scattering of electrons from atomic nuclei are events of this type. The nucleus of even a light atom is thousands of times heavier than the electron; even if the electron were to transfer the maximum momentum to the atom, the large mass difference insures that the kinetic energy imparted thereby would be small compared to the electron's energy. Elastic collisions are the most important source of large-angle scattering. Without such scattering, the beam electrons would brake in almost a straight line; the interaction volume would be a thin "pencil" within the sample along the beam axis. Instead, elastic scattering of the electrons in all directions results in a much broader interaction volume. JMONSEL originally simulated elastic scattering by using Browning's empirical approximation of the Mott elastic cross sections.[8-9] For purposes of simulation, Browning's formula has the virtues of being fast to calculate and defined for all primary electron energies. However, it does represent a smooth interpolation through the empirical data. This means actual cross sections as a function of atomic number may lie somewhat above or below the interpolated values. We have recently added three new options for modeling elastic scattering. One of these uses the NIST Standard Reference Database (SRD) 64, which contains tabulated cross sections determined from the Dirac-Hartree-Fock potential.[10,11] Another uses the tables of Czyzewski et al.[12] A third new option uses a screened Rutherford cross section. For the present study, we used the NIST SRD 64 tables for primary electron energies in the range from 50 eV to 20 keV, where the tables are defined. At energies below 50 eV, we used the Browning approximation as before, but scaled by a constant factor chosen to force agreement with the tabulated value at 50 eV.

Inelastic scattering events are those in which the incident electron loses a non-negligible amount of energy. Sometimes the energetic electron transfers energy to one of the sample's electrons. These are usually the most important inelastic scattering events, events in which the primary electron loses significant energy. The secondary electron (SE) may acquire enough energy to escape the sample, and they can produce more SE by scattering in their turn. This cascade is mainly a low energy phenomenon. The most likely energy transfer in this process is usually in the range of 20 eV to 50 eV, and the cross section is highest for primary electron energies below 100 eV. When the primary electron has energy large compared to the energy loss, these events do not result in a significant change in direction. Thus, these events do not so strongly affect the shape of the interaction volume as do the elastic events described in the previous paragraph. SE significantly outnumber the incident electrons. They are the reason electron yields greater than 1 (more electrons coming out of the sample than going in) are possible at favorable incident energies. The low energies of SE also facilitate efficient collection. For this reason imaging based upon SE is often favored in applications where high throughput is an important consideration, as in most semiconductor industry applications, in particular contour metrology. For this reason, images simulated for the present study were all SE images.

Our model of SE generation is based on the following expression[13] for the many-body differential inverse mean free path:

$$\frac{d^2\lambda_{in}^{-1}}{d(\hbar\omega)dq} = \frac{1}{\pi a_0 E}\mathrm{Im}\left[\frac{-1}{\varepsilon(q,\omega)}\right]\frac{1}{q} \qquad \text{(EQ 1)}$$

with λ_{in} the mean free path between SE generation events, $\hbar\omega$ and q the energy loss and momentum change of the primary electron, a_0 the Bohr radius ($\approx$0.053 nm), E the energy of the incident electron, and $\varepsilon(q, \omega)$ the dielectric function including finite momentum transfer. $\varepsilon(0, \omega)$ is the familiar optical dielectric function. Our implementation of this expression into a Monte Carlo simulator was previously described.[7]

In the present study, we included the thin (approximately 1.3 nm) native oxide layer on our Si samples. This somewhat complicates the simulation because SiO_2, unlike pure Si, has a bandgap large enough that it is possible for an electron to have an energy that is both greater than the potential energy in the vacuum and within a bandgap of the bottom of the conduction band. The first condition means the electron has enough energy to escape the sample. The second means it has too little energy to undergo further energy losses by excitation of SE. Ordinarily, energy loss through excitation of SE is the dominant loss mechanism, but not of course for electrons like these for which such excitations have vanished. To maintain a reasonable description of their energy losses, it is necessary to take into account the next most important loss mechanisms. For this purpose we implemented a model of electron-phonon scattering. The underlying theory is that of Fröhlich.[14] The implementation is similar to that described by Llacer and Garwin[15] and Ganachaud and Mokrani.[16] In this treatment the full expression for the inverse mean free path for phonon excitation is

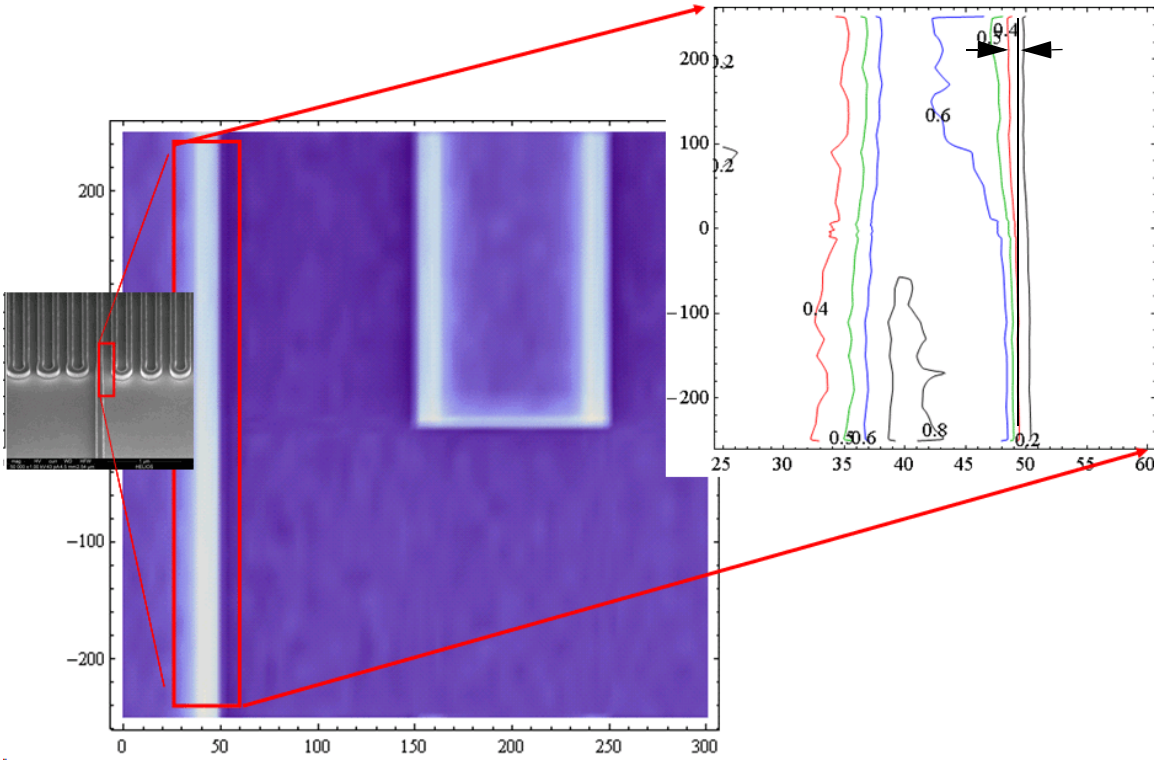

FIG. 6. Modeled isolated/dense contour shifts in AMAG6L pattern. The small image at the left is an oblique-incidence SEM image of the sample upon which the simulated sample was based. The upper part of the sample is periodic with nominally 100 nm lines and spaces. A single line is longer than the others, becoming an isolated line in the lower half of the image. The corresponding modeled image is shown in the middle. The indicated region is drawn as a contour plot at the upper right, with the horizontal axis expanded and the shift of one of the contours indicated.

$$\lambda_{\mathrm{ph}}^{-1} = \frac{n_q + 1}{2}\left(\frac{1}{\varepsilon_\infty} - \frac{1}{\varepsilon_0}\right)\frac{1}{a_0}\frac{E_{\mathrm{ph}}}{E}\ln\left(\frac{1+\sqrt{1-E_{\mathrm{ph}}/E}}{1-\sqrt{1-E_{\mathrm{ph}}/E}}\right) \tag{2}$$

where n_q is an occupation number (close to 0 at room temperature), ε_∞ and ε_0 are the dielectric constants at high and low frequency respectively, a_0 is the Bohr radius, and E_{ph}/E is the ratio of phonon to electron energies. The ratio is almost always quite small for electron energies of interest in our simulations. We take advantage of this to simplify the above expression by keeping only low order terms in the expansion:

$$\lambda_{\mathrm{ph}}^{-1} \approx \frac{n_q + 1}{2}\left(\frac{1}{\varepsilon_\infty} - \frac{1}{\varepsilon_0}\right)\frac{1}{a_0}\frac{E_{\mathrm{ph}}}{E}\ln\left(\frac{4E}{E_{\mathrm{ph}}}\right) \tag{3}$$

A similar expansion of the angular scattering probability is used. This strategy is dropped and the full expressions are used on the rare occasions when E_{ph}/E exceeds 0.1.

On each occasion when a secondary electron or phonon is generated, the primary electron's energy is reduced by an amount equal to the energy of the generated particle. In this way the primary electron slows down via a series of discrete random energy loss events.

The potential energy change at the interface between materials is modeled with the exponential form: $U(x) = \Delta U/(1 - e^{-x/(2w)})$. This form has two parameters, ΔU and w, which represent respectively the change in average potential energy between the two materials and the width over which the change takes effect. For the simulations used here, we assumed w was large compared to the incident electrons' wavelengths. In this limit the transmission probability

of an electron incident on the interface with kinetic energy T at angle of incidence θ reduces to 1 if $T(\cos\theta)^2 \geq \Delta U$ and 0 otherwise. Electrons that fail to transmit are specularly reflected. Those that transmit have their component of momentum normal to the interface altered by an amount that changes the total kinetic energy by ΔU.

3.2 Simulations

The simulated sample contained 21 parallel lines, 200 nm apart. The center line was 1300 nm long. Ten lines to its right and left were each 1000 nm long, with the center line extending 300 nm below the others. All lines were 95 nm high with top width of 80 nm and bottom width 100 nm. Lines were Si with 1.3 nm of surface SiO_2. At each landing position, 4000 normally incident 1 keV electrons were simulated along with their secondary electrons. The signal is comprised of those electrons that escaped the sample with energies less than 50 eV. With $x = 0$ designating the center of the long line and $y = 0$ the bottom edges of the shorter lines (see Fig. 6) all of the simulated landing positions were within the rectangular region with $-0.25\ \text{nm} < x < 300.25\ \text{nm}$ and $-290.25\ \text{nm} < y < 350.25\ \text{nm}$. This region is centered on the iso/dense transition between the longer line and its first neighbor to the right, as shown in Fig. 6. Landing positions were 0.5 nm apart for x or y values within 10 nm of an edge. They were spaced 5 nm apart at positions farther from edges, where the intensity variation with position was slower. Intensities were subsequently interpolated to a uniform grid.

3.3 Edge assignment and results

Edge positions were ascertained by two methods. In the first, which we will call the absolute threshold method, edges were assigned based upon contours of constant SEM signal. This is the method used for the familiar elevation map or contour plot. Contours of constant brightness are shown to the right in Fig. 6. We chose an intensity contour at 45 % of the distance from the global minimum intensity to the global maximum. In the second, which we will call the relative threshold method, the edge in a particular line scan (i.e., along the x direction) was defined as the position where the intensity crossed a threshold midway between the intensity maximum and a fitted baseline value within that line scan (Fig. 7). The same definitions were used for both the simulated and measured images.

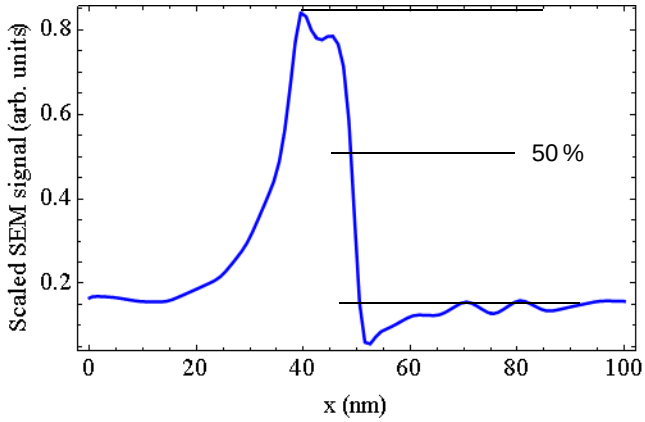

FIG. 7. Edge determination by the relative threshold method. The edge is the position where the intensity crosses a threshold determined by the local maximum and baseline intensities.

With these definitions, the CD change (twice the edge shift) in the simulated image was 1.2 nm for the absolute threshold method and 0.4 nm for the relative threshold method.

4. MEASUREMENTS AND DATA ANALYSIS

Two SEM images were acquired at 1 keV landing energy with an approximately 2.5 µm field of view. One of the images is shown in Fig. 8. Each image was 4096×3775 16-bit pixels. One of them was acquired at 3 µs dwell time and the other at 10 µs.

AFM measurements were obtained using a critical dimension AFM (CD-AFM). CD-AFM is based on technology that was developed by Martin and Wickramasinghe in the early 1990s.[17] The most notable differences are that force sensing in CD-AFM occurs along two axes (one vertical and one lateral) and that the tool uses flared tips which allows imaging of near-vertical sidewalls such as the features found on photomasks. The specific instrument we used for these measurements is a Veeco SXM320[†] installed in our laboratory facilities at NIST. Using NIST methods and samples, we have developed this instrument into a reference measurement system (RMS) for performing traceable measurements of pitch, height, and linewidth.[18-20]

Four CD-AFM images of the isolated/dense transition region of the 200 nm pitch grating were obtained. The CD-AFM software allows the user to select different scan sizes and sampling densities in the fast- and slow-scan axes. All images were obtained using a scan size of 2 µm along the slow-scan axis, which was oriented along the direction of the features. Each image consisted of 80 scan lines distributed evenly along the 2 µm slow-scan axis measurement window. In all four images a fast-scan axis size of 0.5 µm was used, with approximately 1800 to 2200 points distributed over the scan line. Note, however, that due to the two dimensional control algorithm and the scanning of more vertical sidewalls sections in the dense regions, pixel spacing is not uniform.

Two different tips were used during the measurements. Both tips were of circular cross section as viewed from the top. Three images were obtained using a tip that had an estimated width and expanded uncertainty of 77.1 nm ± 1.4 nm. (Uncertainties here and below are reported as ku with u the standard uncertainty and k a multiplier known as the "coverage factor." In this case $k = 2$.) The fourth image was obtained with a different tip that had an estimated width and expanded uncertainty of (95.7 ± 1.2) nm (k =2).

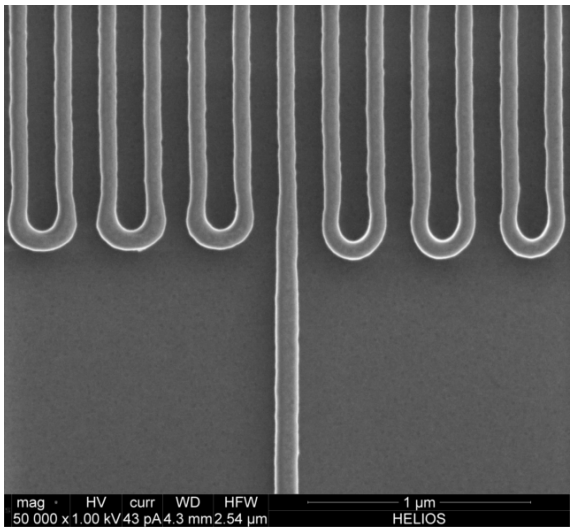

FIG. 8. SEM image of the iso/dense transition region.

A 3-dimensional rendering of one of the four CD-AFM images is shown in Fig. 9. There is a background slope, in particular along the y direction, that is evident in the image. The slope was removed by a background fitting procedure in which two planes with equations $ax + by + c = z$ and $ax + by + c + h = z$ were fit to the substrate and the top surface of the lines. This fit forces the two planes to be parallel. Measured data points were automatically assigned to the upper or lower terrace based upon proximity. Points too far from either plane—mainly those in the walls—were excluded from the fit. The lower plane was subsequently subtracted from all data points to flatten the image.

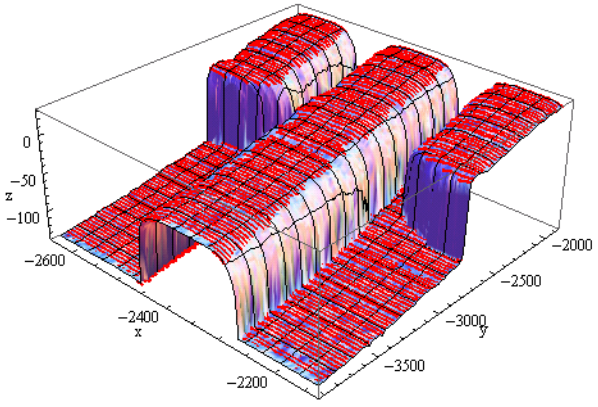

FIG. 9. Three dimensional rendering of CD-AFM data. Points assigned to the upper or lower terrace for the purpose of background fitting are shown in red.

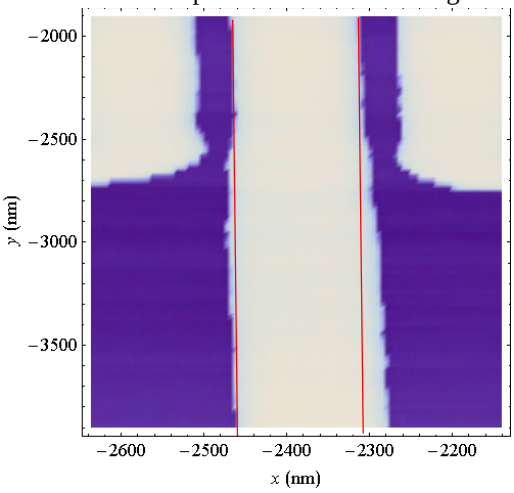

FIG. 10. Top-view rendering of the image after background subtraction. The red lines are extrapolations of the edges in from the upper part of the middle feature.

†. Certain commercial equipment is identified in this paper to adequately describe the experimental procedure. Such identification does not imply recommendation or endorsement by the National Institute of Standards and Technology nor does it imply that the equipment identified is necessarily the best available for the purpose.

A top view of the flattened image is shown in Fig. 10. Parallel red lines extrapolate the edges from the upper dense-neighborhood part of the sample. We have no reason to believe the AFM should be subject to significant neighborhood effects, so the evident greater width of the line in the isolated region must be understood to be real. This is not unexpected. In addition to the SEM metrology differences between isolated and dense neighborhoods, there can be effects in both exposure and development that can lead to real differences in linewidth. This is the reason for doing both SEM and AFM measurements, since the actual edge shifts should be common to both tools while metrology effects differ.

Another measurement artifact is illustrated in Fig. 11. This figure shows the superposition of the two SEM images, with the upper image rendered transparent so the lower one is visible through it. The edges of the central line in one of the images are labeled "1" and "2" for the other image. The edges from the two images align reasonably well near the bottom, but near the top there is wide separation owing to drift of the sample during image acquisition. This drift causes the edges to shift by an amount large compared to the sub-nanometer metrology offset that we expect based upon the modeling. The solution is to compare CD values instead of edge positions. Edge shifts due to sample drift are common mode; they are largely eliminated in the CD measurement because it is differential.

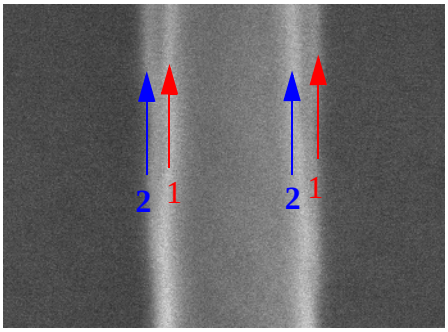

FIG. 11. Superposition of two images, showing drift. The upper image is semitransparent, so the lower image can be seen through it.

If we are to compare the CD-AFM and SEM CD values, it is necessary to align the images so the differences are taken at the corresponding positions. The AFM top image is shown superimposed on the SEM image in Fig. 12. These two image were shifted along the y direction and the correlation between the CD values determined at 1 nm shift intervals. The resulting correlation curve is shown at the right (turned on its side so the offset axis is in the same direction as the *y* axis in the image). The shift that produced the maximum correlation became our initial estimate for the best shift value.

Similarly, if the scales of the two instruments are slightly different, this could produce a difference that might be misinterpreted as a proximity-related error. For example, since there is an approximately 30 nm actual width change between the isolated and dense parts of the line, a 2 % scale error in one tool would lead it to incorrectly assign a value of 30.6 nm to

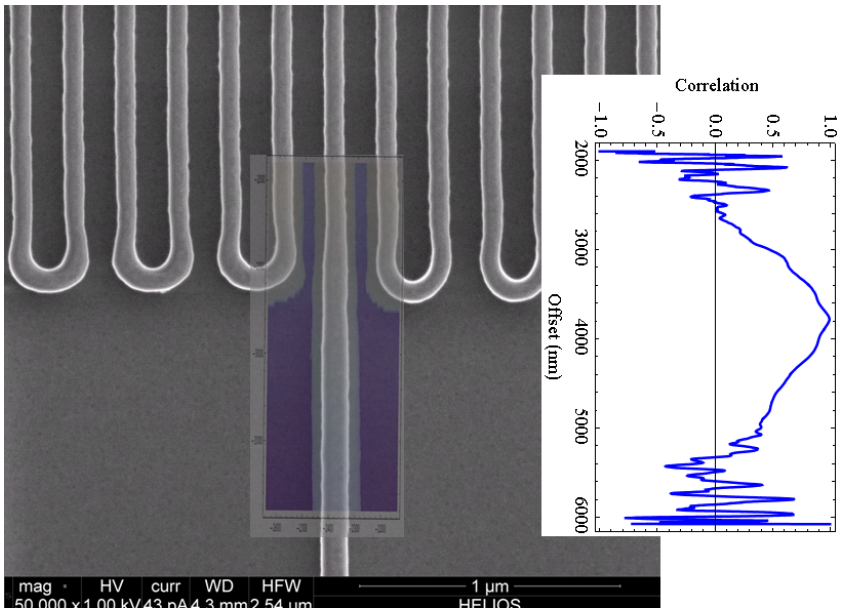

FIG. 12. AFM image overlaid on SEM image. The vertical position is determined by maximizing the correlation between the widths of the central feature.

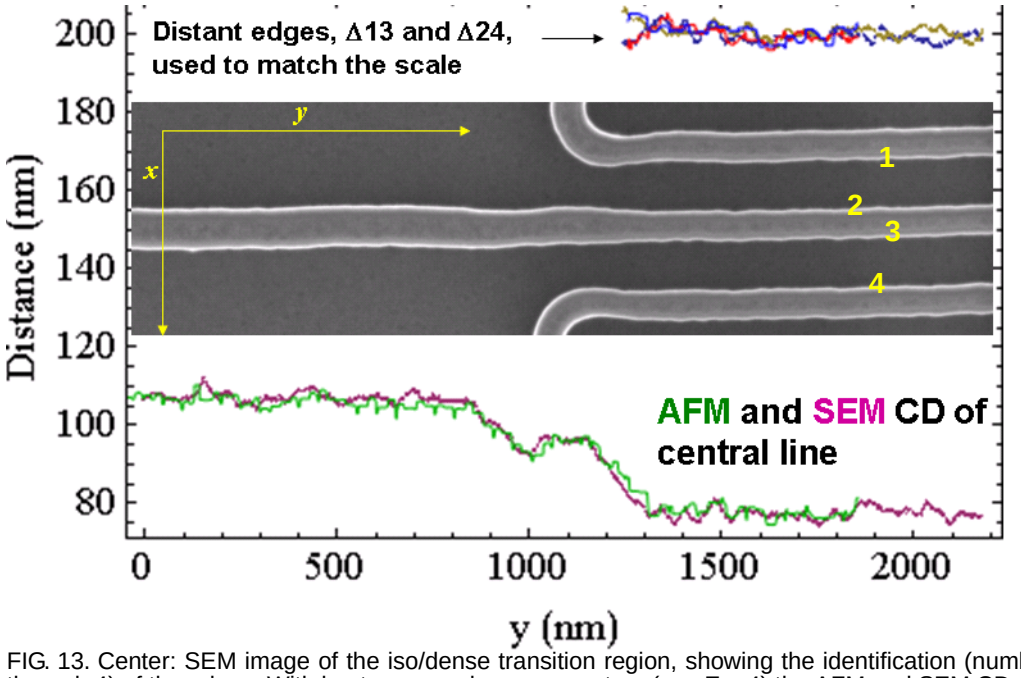

FIG. 13. Center: SEM image of the iso/dense transition region, showing the identification (numbers 1 through 4) of the edges. With best α, y_0, and w_{tip} parameters (see Eq. 4) the AFM and SEM CD values (position differences between edges 2 and 3) match as shown by the two curves at bottom. Similarly, edges 1 to 3 and 2 to 4 match as shown by the four curves at upper right.

this difference. The extra 0.6 nm is significant compared to the size of the metrology error we are led to expect by the modeling. To minimize such scale errors, additional edges from the dense part of the sample are included in our analysis. These additional edges are labeled 1 and 4 in Fig. 13, where the image has been turned on its side. With the inclusion of these edges we form two additional differences, $\Delta 13$ and $\Delta 24$ in each of the images. These are differences between similar (i.e., both right or both left) edges. They should be the same in both tools. The CD (which is $\Delta 23$ in this notation) is a comparison between left and right edges.

The above parameters and corrections may be summarized in this model:

$$\begin{aligned} \mathrm{SEM}\Delta 13(y) &= \alpha \mathrm{AFM}\Delta 13\left(\frac{y-y_0}{\alpha}\right) \\ \mathrm{SEM}\Delta 24(y) &= \alpha \mathrm{AFM}\Delta 24\left(\frac{y-y_0}{\alpha}\right) \\ \mathrm{SEM}\Delta 23(y) &= \alpha \mathrm{AFM}\Delta 23\left(\frac{y-y_0}{\alpha}\right) - w_{\mathrm{tip}} \end{aligned} \tag{4}$$

where *tool*$\Delta ij(y)$ is a function that gives the difference between the ith and jth edges as measured by *tool* at the given y position. The symbols α, y_0, and w_{tip} designate fitting parameters for the scale, y offset, and CD offset respectively. Note that some of these parameters offset and scale the argument of the *tool*Δij function. The best values of the parameters are determined by a least squares fit, with starting values of 1, the y_0 determined from the maximum correlation method described earlier, and the tip size as determined during the CD-AFM measurement.

The result of one such fit is shown in Fig. 13. In this case the edges were assigned by using the absolute threshold method. Natural roughness of the edges and the width change at the transition from isolated to dense provide a robust determination of all parameters. AFM and SEM edges are strongly correlated, with the same roughness features visible in each. Differences between the more distant edges ($\Delta 13$ and $\Delta 24$) are in good agreement between the SEM and AFM. Excluding the transition region, and using only parts of the line where there are available data from both the SEM and AFM images,

the AFM data in Fig. 13 indicate that the isolated part of the line is 30.3 nm wider than the part in the dense neighborhood. The corresponding SEM value is 28.1 nm. The difference between these, 2.2 nm, is attributed to proximity-related error in the SEM measurement.

5. DISCUSSION AND CONCLUSIONS

The above analysis was repeated with the other SEM image and other 3 AFM images. The average value of the iso/dense error was 2.3 nm with a standard deviation of 0.5 nm. Because of the relatively small number of repetitions, we use a coverage factor of $k = 3.2$ (from Student's t table for estimated 3 degrees of freedom) to produce an estimated 95 % confidence interval of 0.7 nm to 3.9 nm. The simulation result (1.2 nm) lies within this interval, but 0 nm does not. We conclude that if the absolute threshold edge assignment is used, simulation and measurement agree that there is a nonzero iso/dense metrology error of one to a few nanometers.

When the relative threshold method of edge assignment was used, the measured mean iso/dense metrology bias was –0.4 nm with a standard deviation of about 1 nm. This produces a 95 % confidence interval of –1.3 nm to 0.6 nm. Once again the simulated value lies within the measurement window, but this time 0 also lies within the window, so the measurement is consistent with there being no proximity-associated error.

The measurements and modeling reported here are based on a single sample. It is possible that other samples will exhibit additional iso/dense effects that were not present in our sample, for example due to differences in charging or in the shapes of line edges between isolated and dense areas. These differences could lead to additional iso/dense metrology errors. For this reason, we feel it is appropriate to interpret a case study like this one as an example of what one might expect in similar cases, but not as defining a rule.

ACKNOWLEDGEMENTS

Prof. Z. J. Ding (University of Science and Technology of Chine, Hefei, Anhui, China) kindly supplied us with scattering tables for Si that had been computed without the single-pole approximation, as described in Reference 6. This project was funded in part by ISMI and in part by the NIST Manufacturing Engineering Laboratory and NIST's Office of Microelectronics Programs.

REFERENCES

[1] J. S. Villarrubia, A. E. Vladár, and M. T. Postek, "A Simulation Study of Repeatability and Bias in the CD-SEM," *J. Microlith. Microfab. Microsyst.* **4**, 033002, (2005). This was a slightly revised update of a paper that first appeared in a conference proceedings, *Proc. SPIE* **5038** (2003).

[2] V. A. Ukraintsev, "Effect of bias variation on total uncertainty of CD measurements," *Proc. SPIE* **5038**, 644-650 (2003).

[3] N. Rana, C. Archie, W. Lu, and B. Banke, "The measurement uncertainty challenge of advanced patterning development," *Proc. SPIE* **7272**, 727203 (2009).

[4] J. S. Villarrubia, N. W. M. Ritchie, and J. R. Lowney, "Monte Carlo modeling of secondary electron imaging in three dimensions," *Proc. SPIE* **6518**, 65180K (2007).

[5] Z.-J. Ding and R. Shimizu, "A Monte Carlo Modeling of Electron Interaction with Solids Including Cascade Secondary Electron Production," *SCANNING* **18**, 92-113 (1996).

[6] S.F. Mao, Y. G. Li, R. G. Zeng, and Z. J. Ding, "Electron inelastic scattering and secondary emission calculated without the single pole approximation," *J. Appl. Phys.* **104**, 114907 (2008).

[7] J. S. Villarrubia and Z. J. Ding, "Sensitivity of SEM width measurements to model assumptions," *J. Micro/Nanolith. MEMS MOEMS* **8**, 033003 (2009).

[8] R. Browning, T. Eimori, E. P. Traut, B. Chui, and R. F. W. Pease, “An Elastic Cross-Section Model for Use with Monte-Carlo Simulations of Low-Energy Electron-Scattering from High Atomic-Number Targets,” *J. Vac. Sci. Technol. B* **9**, pp. 3578-3581 (1991).

[9] R. Browning, T. Z. Li, B. Chui, J. Ye, R. F. W. Pease, Z. Czyzewski, and D. C. Joy, “Empirical Forms for the Electron-Atom Elastic-Scattering Cross-Sections from 0.1 to 30 Kev,” *J. Appl. Phys.* **76**, pp. 2016-2022, Aug. 15 1994.

[10] A. Jablonski, F. Salvat, and C. J. Powell, NIST Electron Elastic-Scattering Cross-Section Database - Version 3.1, National Institute of Standards and Technology, Gaithersburg, MD (2002), http://www.nist.gov/srd/nist64.htm

[11] A. Jablonski, F. Salvat, and C.J. Powell, “Comparison of electron elastic-scattering cross sections calculated from two commonly used atomic potentials,” *J. Phys. Chem. Ref. Data* **33**, p. 409 (2004).

[12] Z. Czyzewski, D. O. MacCallum, A. Romig, and D.C. Joy, “Calculations of Mott scattering cross sections,” *J. Appl. Phys.* **68**, p. 3066 (1990).

[13] D. Pines and P. Nozieres, *The Theory of Quantum Liquids* (Benjamin, New York, 1966).

[14] H. Fröhlich, “Electrons in Lattice Fields,” *Adv. Phys.* **3**, p. 325 (1954).

[15] J. Llacer and E.L. Garwin, “Electron-Phonon Interaction in Alkali Halides. I. The Transport of Secondary Electrons with Energies between 0.25 and 7.5 eV,” *J. Appl. Phys.* **40**, 2766-2775 (1969).

[16] J.P. Ganachaud and A. Mokrani, “Theoretical study of the secondary electron emission of insulating targets,” *Surf. Sci.* **334**, pp. 329-341 (1995).

[17] Y. Martin, H. K. Wickramasinghe, “Method for imaging sidewalls by atomic force microscopy,” *Appl. Phys. Lett.* **64**, 2498-2500 (1994).

[18] N. G. Orji, R. G. Dixson, A. Martinez, B. D. Bunday, J. A. Allgair, and T. V. Vorburger, “Progress on implementation of a reference measurement system based on a critical-dimension atomic force microscope,” *J. Micro/Nanolith. MEMS MOEMS* **6**, 023002-1-10 (2007).

[19] R. Dixson, N. G. Orji, J. Fu, M. Cresswell, R. Allen, W. Guthrie, “Traceable Atomic Force Microscope Dimensional Metrology at NIST,” *Proc. SPIE* **6152**, 61520P-1-11 (2006).

[20] R. Dixson, J. Fu, N. Orji, W. Guthrie, R. Allen, M. Cresswell, “CD-AFM Reference Metrology at NIST and SEMATECH”, *Proc. SPIE* **5752**, 324-336 (2005).